HHS Public Access

Author manuscript

Nat Biomed Eng. Author manuscript; available in PMC 2020 August 03.

Published in final edited form as:

Nat Biomed Eng. 2020 March ; 4(3): 325–334. doi:10.1038/s41551-019-0506-0.

Carbon-coated FeCo nanoparticles as sensitive magnetic-particle-imaging tracers with photothermal and magnetothermal properties

Guosheng Song[1,2,*], **Michael Kenney**[3], **Yun-Sheng Chen**[2], **Xianchuang Zheng**[2], **Yong Deng**[4], **Zhuo Chen**[1], **Shan X. Wang**[4], **Sanjiv Sam Gambhir**[2], **Hongjie Dai**[3], **Jianghong Rao**[2,*]

[1]State Key Laboratory of Chemo/Biosensing and Chemometrics, College of Chemistry and Chemical Engineering, Hunan University, Changsha, Hunan 410082, China

[2]Molecular Imaging Program at Stanford, Department of Radiology, Stanford University School of Medicine, Stanford, California, 94305-5484, USA

[3]Department of Chemistry and Bio-X, Stanford University, Stanford, California 94305, USA

[4]Departments of Electrical Engineering, and Materials Sciences and Engineering, Stanford University, Stanford, CA 94305, USA

Abstract

The low magnetic saturation of iron oxide nanoparticles, developed primarily as contrast agents for magnetic resonance imaging, limits the sensitivity of their detection via magnetic particle imaging. Here, we show that FeCo nanoparticles 10 nm in core diameter bearing a graphitic carbon shell decorated with poly(ethylene glycol) provide a signal intensity for magnetic particle imaging that is about 6-fold and 15-fold higher than the signals from the superparamagnetic iron oxide tracers Vivotrax and Feraheme at the same molar concentration of iron. We also show that the nanoparticles have photothermal and magnetothermal properties and can thus be used for tumour ablation in mice, and that they have high optical absorbance in a broad near-infrared region spectral range (700–1200 nm in wavelength), which also makes them suitable as tracers for

[*]**Correspondence and requests for materials** should be addressed to G. Song or J. Rao. songgs@hnu.edu.cn; jrao@stanford.edu.

Author contributions

G. Song and J. Rao designed the experiments. G. Song performed the experiments. M. Kenney, Z. Chen and H. Dai contributed to the synthesis of nanoalloy. Y. Deng and S. Wang performed the measurement of magnetic saturation of nanoalloy and analysed the data. Y. Chen and S. S. Gambhir contributed to the NIR II photoacoustic imaging and analysed the results. G. Song, X. Zheng and J. Rao analyzed the data and wrote the paper. J. Rao supervised the study.

Competing interests

The authors declare no competing interests.

Supplementary information is available for this paper at https://doi.org/10.1038/s41551-01X-XXXX-X.

Data availability

The main data supporting the findings of this study are available within the paper and its Supplementary Information. All data generated, both raw images and analysed datasets, for the figures in this study are available from figshare with the identifier https://doi.org/10.6084/m9.figshare.10732283.v2.

photoacoustic imaging. As sensitive multifunctional and multimodal imaging tracers, carbon-coated FeCo nanoparticles may confer advantages in cancer imaging and hyperthermia therapy.

In vivo imaging techniques as an invaluable tool enable discovery of new biology in pre-clinical animal models and assist diagnosis of disease and guide treatment in clinics. A number of imaging modalities are available for these biomedical applications, including magnetic resonance imaging (MRI), computed tomography (CT), optical imaging (OI), ultrasound (US), positron emission tomography (PET), and single photon emission computed tomography (SPECT).[1,2] However, it is well recognized that each imaging modality has its own limitations. For example, the photon is generally strongly scattered and absorbed as it penetrates biological tissue even at the near infrared wavelength, which makes it difficult for optical imaging to work in deep tissues non-invasively.[3] MRI contrast agents Gd-chelates are often used to enhance T_1 images but at the sub-mmol concentration.[2] Iron oxide nanoparticles have improved sensitivity as a T_2-MRI contrast agent but the "negative contrast" T_2* images present challenges with working in tissues with intrinsically low MRI signals (and appearing dark) like lung and bone.[4,5] Nuclear imaging such as PET or SPECT has high sensitivity but requires the use of radioactive tracers containing radioisotopes.[3]

In 2005, Gleich and Weizenecker at Philips Research proposed an imaging technology--Magnetic Particle Imaging (MPI)--by using an oscillating magnetic field to image superparamagnetic iron oxide nanoparticles as tracer.[6,7] Unlike MRI measuring the change in nuclear magnetization of water proton, MPI detects the change in electronic magnetization of iron that is 22 million times higher than that of nuclear magnetization of water proton at 7 Tesla. Therefore, MPI promises much higher sensitivity than MRI (7.8 ng of Fe detection has been achieved *in vivo* by MPI).[8] Like PET and SPECT, there is nearly no background signal and no signal attenuation in depth tissue in MPI. The location and concentration of iron oxides nanoparticles can be imaged by MPI anywhere in the body with positive contrast,[7] and the current spatial resolution (about 1 mm) is comparable with PET.[1,7] Unlike PET and SPECT, the MPI tracers do not use radioactivity and have stable reporter activity. Recently MPI have been applied to tracking iron oxide nanoparticles labelled stem cells, macrophages or cancer cells, imaging of vascular, acute stroke, lung perfusion, brain injury, gut bleeding and xenografted tumour in animal model, and even magnetic hyperthermia therapy.[8–21]

Notably, MPI is greatly relying on magnetic nanoparticles as tracer.[6,22,23] Because of the difference in physics between MPI and MRI, iron oxide nanoparticles developed for MRI are not optimal for MPI.[6,22,23] Thus, to unleash the full potential of MPI, it is critical to develop magnetic tracers tailored for MPI. Naturally nearly all MPI studies have been focusing on iron oxide nanoparticles,[1,7,18,24–27] and no efforts have been reported to test whether other magnetic particles than iron oxide can also be MPI tracers.

The MPI physics relies on the nonlinear magnetization curves of small magnetic nanoparticles.[6] The magnetization saturates at the magnetic field strength increases, and high magnetization saturation leads to high MPI signal intensity. Among various magnetic nanoparticles, iron-cobalt (FeCo) nanoparticles show superior magnetic saturation (215 emu/g), compared to other magnetic materials such as Fe_3O_4 (21–80 emu/g), Fe_5C_2 (125

emu/g), and PtFe (100 emu/g) nanoparticles.[5,28–31] Therefore, FeCo nanoparticles appeared to us attractive as a potentially good MPI tracer. In this work, we demonstrate the use of carbon-coated FeCo nanoparticles as a non-iron oxide based MPI tracer. We have investigated the effects of the metal core composition and the size of particles on the MPI signal intensity, and found that FeCo@C nanoparticles with a core size of 10 nm in diameter produced MPI signal 6.08 times that of Vivotrax (a commercial MPI tracer) and 14.91 times that of Feraheme at the same core molar concentration. To our best knowledge, this value represents the most sensitive MPI tracer reported so far, even the particle core is just 10 nm in diameter and much smaller than the calculated size expected for an MPI-tailored iron oxide nanoparticle (larger than 20 nm). They also possess high r_2 relativities and strong near-infrared absorbance that enable MRI and second near-infrared II (NIR-II) photoacoustic imaging (PAI). After intravenous injection, FeCo@C-PEG efficiently accumulated in tumours (5.7% ID/g tissue) and significantly enhanced the MPI signal in tumours by 10-fold. Furthermore, FeCo@C-PEG nanoparticles showed efficient photothermal and magnetic hyperthermia effects, which were successfully applied for image-guided thermal ablation of solid tumours *in vivo* in a mouse model of breast cancer. This multimodal theranostic nanoparticle (Scheme 1) may find applications for both imaging-based disease diagnosis and imaging-guided cancer therapy.

Results

Synthesis and characterization of FeCo@C nanoparticles for MPI

Bare FeCo nanoparticles are not stable in air and will be quickly oxidized. To stabilize the particle, a graphitic carbon shell was introduced against oxidation and chemical reactions in air and liquid phases. We prepared FeCo@C nanoparticles by methane chemical vapor deposition (CVD).[28] First, iron nitrate and cobalt nitrate was loaded into fumed silica powder by impregnation in methanol solution. The dried metal-loaded silica was heated to 800 °C in a CVD device under a H_2 flow to form FeCo alloy nanoparticles, and then subjected to methane flow at 800 °C for carbon deposition on FeCo nanoparticles. Once cooled down, the sample was etched in HF to dissolve silica and collected by centrifugation. The resulted FeCo nanoparticles were coated with a graphitic carbon shell (FeCo@C), further modified by an amphiphilic copolymer PEG-grafted poly(maleicanhydride-alt-l-octadecene) (C18PMH-PEG) (PEG MW of 5,000) via hydrophobic interactions.[32] The resulting polymer-modified nanoparticles (FeCo@C-PEG) were dispersed well in H_2O and 1 x PBS.

To test the effect of the reaction parameters of nanoparticle synthesis on their MPI signals, we first fixed the mole ratio of Fe and Co precursor at 1: 1, and varied the mass ratio of silica to metal from 4: 1, 2: 1 to 1: 1. After modification by C18PMH-PEG, the resulting particle suspensions were centrifuged to remove large aggregates. The iron and cobalt concentrations of particles were measured by inductively coupled plasma mass spectrometer (ICP-MS). Their MPI signals were measured with a MPI scanner (MOMENTUM™ Imager, Magnetic Insight Inc.). In order to evaluate their MPI sensitivity relative to Vivotrax (MPI commercial tracer), the core mass (containing both Fe and Co) was normalized to 1 μg, and compared to Vivotrax at 1 μg of Fe and O. As shown in Table 1, the mass ratio of silica to

metal at 1: 1 gave the highest MPI signal among three samples--2.4-fold of that of Vivotrax. Then, the mass ratio of silica to metal was kept at 1: 1, and the mole ratio of Fe: Co was varied from 1: 1 to 2: 1 and 1: 2. The MPI measurements of these samples indicated that the mole ratio of Fe to Co precursor at 1: 1 afforded the highest MPI sensitivity (Sample #3 in Table 1).

To understand the effect of the particle size on the MPI sensitivity, we took advantage of the fact that the nanoparticles prepared by the CVD method usually had a wide size distribution. We analysed sample #3 by the density gradient rate (DGR) separation method to separate nanoparticles by their sizes.[33,34] FeCo@C-PEG aqueous solution was added into the density gradient solution containing 10%, 20%, 30%, and 40% of iodixanol for centrifugation. The as-synthesized FeCo@C-PEG nanoparticles were separated in gradient layers after centrifugation and five fractions were manually collected for characterization by transmission electron microscope (TEM, JEM-1230, 120 kV) (Supplementary Fig. 1a–f), ICP-MS and MPI (Table 2). The average diameters of fractions #1 to #4 gradually increased from 5.3 nm to 12 nm, as revealed by TEM (Supplementary Fig. 1b–e). Fraction #5 contained the aggregated nanoparticles with a large size (Supplementary Fig. 1f). As shown in Table 2, both nanoparticles' size and metal ratio could have an effect on the MPI signal of FeCo@C-PEG. For example, fractions #2, #4, #5 had a close molar ratio of Fe to Co (from 1: 0.69 to 1: 0.73), but smaller FeCo@C-PEG nanoparticles showed higher MPI signals than larger particles: fraction #2 (7.1 nm) > fraction #4 (12.1 nm) > fraction #5 (15.9 nm). It is interesting to note that for MPI-tailored iron oxide nanoparticles, the preferred particle size was reported to be around 25–26 nm.[17] This difference may reflect the unique property of FeCo nanoparticles and warrants further investigation. On the other hand, the MPI signal for fraction #3 had the highest metal ratio of Fe to Co (1: 0.87), and also the highest MPI signal--3.51 times of Vivotrax at the same mass of core. The trends observed in both Table 1 and 2 suggest that an optimal combination of the molar ratio of Fe to Co and the size of the particle core of FeCo@C-PEG nanoparticles is key to achieving high MPI sensitivity.

High-resolution TEM (FEI Tecnai F20, 200 kV) analysis of fraction #3 particles clearly showed the lattice fringes in the FeCo nanocrystal with d-spacing of 2.0Å, corresponding to crystalline face (1 1 0) (Fig. 1a). The high-angle annular dark-field scanning TEM (HAADF-STEM) imaged Fe and Co elements in the particle (Fig. 1b). X-ray diffraction (XRD, Shimadzu XRD-6000) confirmed cubic-FeCo crystalline structure of the nanocrystal (PDF#49–1567) (Fig. 1c). Importantly, no metal-carbide phase could be observed in the XRD pattern, indicating that the deposited carbon mainly interacts with nanoparticle's surface to form an encapsulating graphitic shell.[28] Raman spectroscopy showed G peak (~1,578 cm^{-1}) and D peak (~1,328 cm^{-1}) (Fig. 1d), consistent with a graphitic carbon shell coated onto the surface of FeCo nanocrystals.[35] Magnetic hysteresis curves were measured by a MicroMag™ (Model 2900, AGM) at room temperature, indicating that FeCo@C was superparamagnetic at room temperature with no hysteresis loop (Fig. 1e). With the total metal mass of FeCo@C determined by ICP-MS, the saturation magnetization (Ms) of FeCo@C was calculated to be 192 emu/g, much higher than that of Vivotrax (54 emu/g). The chemical stability was measured by ICP-MS and less than 2% of Co was released from FeCo@C-PEG after 7 days' incubation in 1 x PBS (pH=4.4), suggesting high chemical stability in acidity by the graphitic carbon shell (Supplementary Fig. 2). Moreover, after

incubation in 1 x PBS (pH=7.4) for 10 days, little decrease in the MPI signal was observed for FeCo@C-PEG, indicating the carbon coating was robust enough to prevent metal from oxidation of FeCo (Supplementary Fig. 3). The dynamic light scattering (DLS) measurement of FeCo@C-PEG reported a hydrodynamic size of about 40 nm in water and 1 x PBS (Fig. 1f) and no notable size changes even after 7 day's incubation (Supplementary Fig. 4), demonstrating the PEG coating sufficiently strong to ensure good dispersion in biological media.

The graphitic carbon shell of FeCo@C-PEG afforded it high absorbance in the near-infrared region (between 700 and 1200 nm) (Fig. 1g). In the NIR II range (1000–1200 nm), tissue produces less optical scattering and absorption than in the NIR I (650–900 nm) window. However, only a few types of nanoparticles have optical absorption in the NIR II. The broad optical absorption spectrum of our nanoparticles extends to NIR II, making it potentially a good NIR photoacoustic imaging contrast agent that can work for both NIR I and NIR II windows. The metal mass (Fe and Co) extinction coefficient of FeCo@C-PEG was calculated to be 8.96 g^{-1} L cm^{-1} at 800 nm and 6.48 g^{-1} L cm^{-1} at 1064 nm (Fig. 1h). The corresponding metal molar (total Fe and Co) extinction coefficient was 515 M^{-1} cm^{-1} at 800 nm, and 373 M^{-1} cm^{-1} at 1064 nm. For photoacoustic imaging or photothermal therapy, the key parameters for agents are the photoconversion efficiency and stability. To calculate the photothermal conversion efficiency (n), FeCo@C-PEG aqueous solution was irradiated under 808 nm laser (1 W/cm^2) until the temperature increase reached a steady state, and then naturally cooled down (Supplementary Fig. 5).[36] The photothermal conversion efficiency was calculated to be 26.7%, which was comparable to the reported values for Au nanorods (23.7%) and Cu_9S_5 nanocrystals (25.7%).[37] Moreover, FeCo@C-PEG demonstrated excellent photoconversion stability under repeated irradiation of 808 nm laser, which is superior to indocyanine green (ICG) and Au nanorods (Supplementary Fig. 7).

Next, we compared FeCo@C-PEG with the iron oxide particles, commercial MPI contrast agent (Ferucarbotran, Vivotrax) and commercial MRI contrast agent (Ferumoxytol, Feraheme) for MPI study. FeCo@C-PEG, Vivotrax and Feraheme (each containing 800 ng of core) in PCR tubes were scanned by MPI (Supplementary Fig. 8). The 2-D projection MPI image of FeCo@C-PEG showed much higher contrast than Vivotrax and Feraheme (Fig. 2a): compared at the same core mass concentration, the MPI signal of FeCo@C-PEG is 3.5 times that of Vivotrax and 8.6 times that of Feraheme (Fig. 2b); if compared at the same molar core concentration, the MPI signal of FeCo@C-PEG is 6.08 times that of Vivotrax and 14.91 times that of Feraheme. Moreover, MPI signals of FeCo@C-PEG are linearly dependent on the nanoparticles' concentration (core mass) with a slope of FeCo@C-PEG (47.6 μg^{-1}) much higher than that of Vivotrax (13.2 μg^{-1}) (Fig. 2c). FeCo@C-PEG (12.5 ng of metal core) gave a signal-to-background ratio of 1.29 in one MPI scan, calculated from MPI spectrum (Supplementary Fig. 9). While the endogenous background of MPI is very low, we found that there was a very low-level background signal from the instrument including the imaging stage. It may be subtracted to further increase the signal-to-background ratio. The scan number may also be increased to improve imaging sensitivity. For example, PCR tubes containing FeCo@C-PEG (10 and 5 ng of the metal core) were scanned by 2D Average / Time Course MPI with 25 times scanning (Supplementary Fig. 10a,c). After subtraction of the background signal pre-acquired without the sample, 10 ng

and 5 ng of FeCo@C-PEG can be imaged on MPI with the signal-to-background ratio of 2.26 and 1.36, respectively (Fig. 2d,e and Supplementary Fig. 10b,d), demonstrating excellent sensitivity of FeCo@C-PEG for MPI. The spatial resolution of FeCo@C-PEG for MPI was measured in phantom.[13] Two tubes with an edge-to-edge distance of 3.1 mm were well separated in a 2-D projection MPI image (Supplementary Fig. 11). Owing to the high saturation magnetization of FeCo@C-PEG, we measured the conversion efficiency from magnetism to heat (Fig. 2f, and Supplementary Fig. 12). FeCo@C-PEG solution (4 mg/mL) could be heated to 37 °C from 25 °C in 5 min by a magnetic hyperthermia coil setup (100 kHz, 15 KVA), while Vivotrax only increased by 3 °C (Fig. 2f). The specific absorption rate (SAR) is defined as the absorbed energy per material mass and calculated by the Equation in Supplementary Table S1.[39] From the temperature curves (Supplementary Fig. S12b), the SAR of magnetic hyperthermia for FeCo@C-PEG was measured to be 406 W/g, which is 4.83 times of Vivotrax and 1.53 times of Fe_3O_4 (Supplementary Table S1), suggesting high efficacy of FeCo@C-PEG for magnetic hyperthermia.

MPI imaging of cancer xenografts in mice with FeCo@C-PEG

The cytotoxicity of FeCo@C-PEG was evaluated by MTT assay, and no obvious toxicity to murine breast cancer 4T1 cells was observed at as high as 200 μg/mL of FeCo@C-PEG (Supplementary Fig. 13). Next, in order to investigate whether FeCo@C-PEG was able to exert MPI performance *in vivo,* FeCo@C-PEG and Vivotrax (each 20 μL at 35 μg/mL) were directly injected into tumours (murine breast cancer 4T1) of living mice separately for 2-D projection MPI scanning. The tumour injected with FeCo@C-PEG showed high contrast in MPI images (Fig. 3a,b), which was about 3.5 times of the signal from Vivotrax (Fig. 3b) (P = 0.00041). As expected, when imaged from different positions by 2-D projection MPI scanning, the MPI signals from the tumour areas varied little (Fig. 3c,d), demonstrating that MPI is not subject to tissue depth attenuation (Fig. 3d). 3-D MPI images were acquired in fusion with CT, MPI/CT to produce tomographic MPI images of the tumour (Supplementary Fig. 14).

We further evaluated the potential of FeCo@C-PEG for MPI cancer imaging *in vivo* after systemic introduction into the body. The Balb/c mice bearing 4T1 xenograft breast tumours were intravenously injected with FeCo@C-PEG (3 mg/kg), and scanned by 3-D CT and MPI coronally, sagittally, and axially (Fig. 3e,f and Supplementary Fig. 15) 24 hours post-injection. In addition to strong MPI signals from the abdomen area due to non-specific uptake of FeCo@C-PEG by liver and spleen, nanoparticles preferentially accumulated into tumours due to the enhanced permeability and retention (EPR) effect (Fig. 3g). The MPI signals of tumour areas significantly increased by 10 times after injection of FeCo@C-PEG (Fig. 3h,i) (P = 0.00012). In comparison, MPI signals of tumour areas showed no obvious changes after intravenous injection of Vivotrax (3 mg/kg) (Fig. 3h,i), due to the weak EPR effect.[40] The tumour-to-normal tissue ratio was calculated to be 4.76 and 1.33 for FeCo@C-PEG and Vivotrax, respectively (Supplementary Fig. 16) (P = 0.0003). After imaging, the mice were sacrificed and major organs were collected for MPI imaging. Because the MPI signal of FeCo@C-PEG is linear to its concentration, the mass of FeCo@C-PEG in each organ can be quantitated by MPI signals. The tumour uptake for FeCo@C-PEG was calculated to be 5.7% ID/g, at 24 hours post injection, while the tumour uptake for Vivotrax

was only 0.64% ID/g (Fig. 3j), These results showed that FeCo@C-PEG was superior to Vivotrax for *in vivo* tumour imaging. The biodistribution of FeCo@C-PEG in tumour was further confirmed by ICP-MS and Bio-TEM (Supplementary Fig. 17, 18).

In order to investigate MPI imaging ability of deep-located tumour, the mice bearing orthotopic glioma tumour model was prepared [41] and i.v. injected with FeCo@C-PEG (9 mg/kg) (Supplementary Fig. 19). MPI/CT clearly visualized tumour at 4 hours post-injection (Supplementary Fig. 19b), which was confirmed by the bioluminescence imaging and histopathologic analysis (H&E staining) (Supplementary Fig. 19a, c). The quantification showed the MPI signals of marked tumour areas increased 5.1 times after injection (Supplementary Fig. 19d) ($P = 0.0011$).

FeCo@C-PEG for MRI and photoacoustic imaging

In order to investigate the MRI contrast ability, we measured the relaxation times (T_2) of protons in water solutions of FeCo@C-PEG in a 1.5 T magnetic field (MQ 60 scanners at 37 °C), and compared with Feraheme (Fig. 4a). FeCo@C-PEG exhibited higher r_2 (11.74 s^{-1} mg^{-1} L) than that of Feraheme (1.15 s^{-1} mg^{-1} L) at 1.5 T; If calculated by the mole concentration of metal, the r_2 of FeCo@C-PEG is 669.32 $s^{-1}mM^{-1}$, while the r_2 of Feraheme is 64.61 s^{-1} mM^{-1}. The large r_2 value of FeCo@C-PEG prompted us to further examine the MRI ability of FeCo@C-PEG *in vivo.* The mice received intravenous injection of FeCo@C-PEG (3 mg/kg) was imaged by T_2-MRI (MR solution, 3T) for comparison (Fig. 4b). The tumour exhibited enhanced negative contrast (Fig. 4b), and the MRI intensity of the tumour region decreased from 1770 to 622 after injection (Fig. 4c) ($P = 0.0054$).

The NIR-II photothermal conversion ability of FeCo@C-PEG was measured via an infrared camera (Supplementary Fig. 20). Under irradiation of 1064 nm NIR laser (1.0 W/cm^2) for 5 min, the temperature of FeCo@C-PEG solution (220 μg/mL) increased from 27 °C to 42 °C, while the temperature of pure water only increased by 3 °C, indicating the efficient NIR-II photothermal effect (Fig. 4d). From the temperature curves (Fig. 4d), the SAR of photothermal hyperthermia for FeCo@C-PEG (20 μg/mL) was calculated to be 14700 W/g, which was comparable to the reported Au nanorods[39] (Supplementary Table S2). The strong photothermal conversion ability makes FeCo@C-PEG a good photoacoustic contrast agent in the NIR-I and NIR-II regions.

As a hybrid imaging modality that uses laser light to excite the sample and produce acoustic signals for imaging, PA imaging still faces the limitation of depth penetration but provides higher spatial resolution than MPI.[1,42–44] The longer wavelengths of excitation lasers, the larger depth penetration.[42,45] We evaluated FeCo@C-PEG for PA imaging at both 800 nm and 1064 nm of the mice bearing 4T1 tumours (Fig. 4e and Supplementary Fig. 21). While the light absorbance efficiency of FeCo@C-PEG at 800 nm was higher than that at 1064 nm (Fig. 1h), the average PA signals of tumour area at 1064 nm was comparable to that imaged at 800 nm (Fig. 4f), probably due to the better penetration and lower scattering of 1064 nm laser. These results demonstrate the potential of FeCo@C-PEG nanoparticles as a contrast agent for both MRI and PA imaging.

To investigate the imaging ability of FeCo@C-PEG for small tumours, mice bearing 4T1 tumours (about 4 mm) were i.v. injected with FeCo@C-PEG (3 mg/kg) (Supplementary Fig. 22a). Photoacoustic and axial MPI/CT imaging showed high contrast within tumour areas at 24 hours post injection (Supplementary Fig. 22b,c). The MPI signals of tumour increased by 7.2 times after injection (Supplementary Fig. 22d) ($P = 0.00064$).

FeCo@C-PEG as hyperthermia nanoparticles for tumour ablation

Among therapeutic approaches of cancer, magnetic hyperthermia and photothermal therapy can result in thermal ablation of tumour.[46] Owing to the strong photothermal conversion effect, we examined the heating effect of FeCo@C-PEG *in vivo* on mice bearing 4T1 tumours. When exposed to 1064 nm continuous laser (1.0 W/cm^2), the tumours injected with FeCo@C-PEG could rapidly heat tumours to 54 °C within 10 min (Fig. 5a,b). As a control, the tumour injected with 1 x PBS showed little temperature rising under the same irradiation (Fig. 5a,b). The difference of tumour temperature is consistent with the *in vitro* results (Fig. 4d). To evaluate the NIR-II photothermal therapeutic efficacy, mice bearing 4T1 tumours received the following treatment: (1) 1 x PBS, (2) NIR (1064 nm laser only, 1.0 W/cm^2, 10 min), (3) FeCo@C-PEG only (i. t. injection, 50 μl, 2 mg/mL), and (4) FeCo@C-PEG (i. t. injection, 50 μl, 2 mg/mL) + NIR (1064 nm laser, 1.0 W/cm^2, 10 min). The tumour growth curves showed that tumours treated with FeCo@C-PEG + NIR (group 4) were greatly suppressed and showed little growth within 14 days (Fig. 5c and Supplementary Fig. 23a). As a comparison, the tumour treated with laser irradiation only (group 2) and FeCo@C-PEG injection only (group 3) showed a growth profile similar to the 1 x PBS treatment group (group 1).

Subsequently, we explored the magnetic hyperthermia therapy *in vivo.* The infrared thermal images showed that the tumour directly injected with FeCo@C-PEG (100 μg or 250 μg) could be quickly heated from 30 °C to 41 °C or 47 °C, respectively, within 10 min, under the heating of magnetic hyperthermia coil setup (SP-15A, 100 kHz, 15 KVA), while the tumour injected with 1 x PBS only increased from 30 °C to 32 °C (Fig. 5d,e; Supplementary Fig. 24). Mice bearing 4T1 tumours were divided into four groups (n = 5) and treated with (1) 1 x PBS, (2) only magnetic field (100 kHz, 15 KVA), (3) only FeCo@C-PEG only (i. t. injection, 50 μL, 5 mg/mL), (4) FeCo@C-PEG (i. t. injection, 50 μL, 5 mg/mL) and magnetic field (100 kHz, 15 KVA). The tumour growth curves showed that FeCo@C-PEG + magnetic field (group 4) was able to greatly inhibit the tumour growth than that treated with magnetic field only (group 2) or FeCo@C-PEG injection only (group 3) (Fig. 5f and Supplementary Fig. 23b). Moreover, histological examination of tumours treated with FeCo@C-PEG + magnetic field showed obvious karyorrhexis, karyolysis, and pyknosis, suggesting the effective magnetic hyperthermia ablation of solid tumour using FeCo@C-PEG (Supplementary Fig. 25). In comparison, no obvious necrosis was observed in tumours treated with only FeCo@C-PEG or magnetic field. In addition, no obvious body weight changes were observed among groups during photothermal or magnetic hyperthermia therapy (Supplementary Fig. 26a&b).

Furthermore, the *in vivo* toxicity of FeCo@C-PEG was tested by the hematology analysis, blood biochemistry and histological examination (Supplementary Fig. 27, 28). After i.v.

injection of FeCo@C-PEG (15 mg/kg), the main indexes of blood biochemistry and hematology exhibited no obvious abnormalities on the 1st, 7th, 14th, 28th day, compared with those of untreated healthy mice (Supplementary Fig. 27). Moreover, the histological examination of major organs in FeCo@C-PEG treated mice at measured days revealed no apparent histopathological abnormalities or lesions (Supplementary Fig. 28). Besides, the biodistribution of FeCo@C-PEG was measured via ICP-MS to determine Co contents in various organs and showed gradual clearance from liver and spleen during 28 days post i.v. injection (Supplementary Fig. 29). Therefore, our results demonstrated no apparent toxicities induced by FeCo@C-PEG at our tested condition *in vivo*.

Discussion

MPI as a *in vivo* imaging modality has superior advantages over other *in vivo* imaging technologies for disease diagnosis and treatment monitoring, for example, no signal attenuation in tissue, tomographic imaging capability, nearly no background from biological tissues, positive contrast similar to nuclide imaging but with no ionizing irradiation, and linear correlation between imaging signal and the quantity of tracers. Importantly, MPI has been suggested to offer excellent sensitivity--a possible detection limit of 20 nM of Fe, but this potential has been largely limited by the lack of MPI-tailored magnetic nanoparticle tracers. Until now all MPI tracers are made of iron oxide nanoparticles, and there are no other kinds of nanoparticles reported for MPI.[8–19] The high magnetism of FeCo alloy nanoparticles motivated us to investigate its potential for MPI. We developed the synthetic and purification method to probe the effect of composition and size of FeCo nanoparticles on their MPI signal sensitivity. FeCo nanoparticles synthesized with an optimized composition and size possess much higher MPI signals than Vivotrax and Feraheme (iron oxides based MPI tracers) compared at the same mass of the core.

The superior saturation magnetization (192 emu/g) not only endows FeCo@C-PEG with high MPI signal, but also 10 times of r_2 relaxation in T_2-MRI than that of Feraheme. Moreover, the superior magnetic property of FeCo@C-PEG promoted us to explore the magnetothermal effect for hyperthermia tumour ablation. Interestingly, FeCo@C-PEG could produce strong hyperthermia effects with rapid increase in the solution temperature under the magnetic field, and thereby have effective magnetic hyperthermia ablation of solid tumour. Since magnetic hyperthermia is not limited by tissue penetration, and can be repeated in multiple hyperthermia cycles, it has high potential for clinical translation for the treatment of solid tumours.[10,46]

To enhance the stability and biocompatibility of the FeCo nanoparticles, a carbon-coating shell was introduced for surface-anchoring of amphiphilic polymers. Notably, the carbon coating endowed FeCo nanoparticles with high chemical stability resistant to acidity and oxidation. Furthermore, the carbon coating afforded another attractive feature-broad absorbance to the NIR II region. NIR II is of growing interest because of improved tissue penetration depth and low background signal and light scattering in biological tissues in compared with the traditional first NIR (NIR I) region.[45,47,48] Moreover, FeCo@C-PEG possessed higher photoconversion efficiency and stability, compared with that of commonly used photoacoustic nanomaterials (Au nanorods). We have demonstrated that FeCo@C-PEG

can allow both photoacoustic imaging (PAI) and photothermal therapy (PTT) using NIR-II (1064 nm) laser.

Since a single modality is rarely adequate to provide enough evidence for disease diagnosis in clinic use,[1,49] single nanoparticles for multimodality imaging are thus particularly attractive. MRI is able to provide anatomical structure information of soft tissues with high spatial resolution. With its superb sensitivity and positive contrast, MPI offers complementary imaging in overcoming low sensitivity and negatively enhanced contrast of MRI by iron oxide nanoparticles. Such high sensitivity, positive contrast, and no penetration limit make FeCo@C-PEG extremely suitable for biosensing and detection of biomarker *in vivo,* via MPI imaging. PAI maintains even higher spatial resolution and rich contrast in superficial tissues. The integration of contrast enhancing capability for MRI, MPI and PAI into a single nanoparticle makes FeCo@C-PEG a unique, powerful imaging agent.

In our demonstration of cancer imaging and hyperthermia therapy with FeCo@C-PEG, FeCo@C-PEG nanoparticles passively accumulated at tumours through the EPR effect or direct injection. Many tumour-homing ligands including peptides, antibodies, and small molecules may be introduced to FeCo@C-PEG through chemical functionalization to improve specificity for tumour imaging and hyperthermia therapy.

Future research in the FeCo nanoparticle synthesis may further improve their magnetic properties and thereby MPI signals, for example, varying particle size (from 10 to 50 nm), tuning crystalline structure and reaction conditions.[50] This work demonstrates the feasibility of designing MPI tracers beyond iron oxides. Other types of magnetic particles, such as $AuFe_3$, FePt, $Nd_2Fe_{14}B$, Fe, Fe_5C_2, and FeS nanoparticles, may also be explored in search for more sensitive MPI tracers.

From the long-term biodistribution (Supplementary Fig. 29), FeCo@C-PEG may be slowly cleared through the hepatobiliary route like many other nanoparticles.[51,52] Despite the slow clearance of FeCo@C-PEG from liver and spleen post i.v. injection, no evidence of toxicity from *in vitro* cytotoxicity data, complete blood panel, blood biochemistry analysis and histological examination results was found within our tested dose and time range. Those results suggested that our FeCo@C-PEG is relatively safe, although more toxicological evaluation is needed in future.

In summary, FeCo@C nanoparticles possessed high saturation magnetization of the FeCo core and strong optical absorbance of the carbon shell, and exhibited strong MPI signal, high r_2-MRI relaxivity, and NIR-I and NIR-II photoacoustic imaging capability. Our results have demonstrated FeCo@C-PEG as a cancer imaging contrast agent for MPI, T_2-MRI, NIR-II photoacoustic and thermal imaging. The synthesized FeCo@C-PEG displayed excellent chemical stability, colloid stability, photostability, and biocompatibility. Furthermore, FeCo@C-PEG could produce rapid temperature increase in the magnetic field for magnetic hyperthermia therapy, and by NIR-II laser irradiation for efficient photothermal ablation of tumour, with deep tissue penetration and low normal tissue damages. Thus, the multiple functionalities of FeCo@C-PEG nanoparticles for integrating multimodal *in vivo* imaging

and magnetic/photo induced hyperthermia therapy should make these nanoparticles advantageous and efficient for cancer imaging and hyperthermal treatment.

Methods

Synthesis of FeCo@C nanoparticles:

FeCo@C was synthesized according to previously published procedure.[28] Typically, 0.72 mmoL of iron (III) nitrate nonahydrate, 0.72 mmoL of cobalt (II) nitrate hexahydrate and 0.5 g of fumed silica were dissolved in 50 mL of methanol and sonicated for 1 hour. After removing methanol and drying at 80 °C, the powder of silica loaded with metal was grounded and placed in a tube furnace for methane chemical vapor deposition (CVD). The sample was heat to 800 °C in a H_2 flow (100 cm^3 / min) and Ar flow (250 cm^3 /min), and then subjected to a methane flow (350 cm^3 / min) for 5 min. Once cooled down, the sample was etched with water containing HF (10%) and ethanol (10%) to remove the silica overnight. FeCo@C was collected by centrifugation at 8000 rpm for 10 min and then washed with H_2O for several times.

Surface modification of FeCo@C nanoparticles:

FeCo@C nanoparticles were modified with PEG-grafted poly (maleic anhydride-alt-1-octadecene) (C18PMH-PEG).[32] FeCo@C was added into 10 mg/mL of C18PMH-PEG and sonicated for 1 hour, followed by centrifugation at 3,000 rpm to remove any aggregates. C18PMH-PEG was synthesized as previously described.[32] The excess C18PMH-PEG was removed by ultrafiltration. The resulted FeCo@C-PEG aqueous solution was stored in 4 °C for later use.

Separation of FeCo@C-PEG:

FeCo@C-PEG was separated by density gradient rate (DGR) separation method, according to our previous work.[33] 10%, 20%, 30%, and 40% of iodixanol aqueous solution was successively added into centrifuge tube to form a four-layer gradient solution. 0.2 mL of FeCo@C-PEG aqueous solution was added onto the top of the four-layer aqueous iodixanol solution, and centrifuged at 12,000 rpm (17,000 g) for 100 min. The gradient solution containing separated nanoparticles was manually fractioned from the centrifuge tube for characterization.

Cell culture:

Murine breast cancer cells (4T1) were obtained from American Type Culture Collection (ATCC) and human glioma cancer U87-luciferase cells were obtained from PerkinElmer. Those cells were cultured in normal RPMI-1640 or DMEM culture medium with 4.5 g / L of D-glucose (containing 10 % of fetal bovine serum and 1% of penicillin/streptomycin) at 37 °C under 5 % CO_2.

In vitro cytotoxicity test:

4T1 cells pre-seeded into 96-well plates (1×10^5 / well) were incubated with various concentrations of FeCo@C-PEG for 24 hours. A standard methyl thiazolyltetrazolium (MTT, Sigma, M5655) assay was used to determine cell viability.

Tumour model:

All animal experiments were carried out in compliance with the Guidelines for the Care and Use of Research Animals established by the Stanford University Animal Studies Committee and by the Institutional Animal Care and Use Committee of Hunan University. Balb/c female white or nude mice (20 ± 2g) were obtained from Charles River (USA) or Hunan SJA Laboratory Animal Co. Ltd. (China). Female Balb/c mice were subcutaneously injected with 4T1 cells (50 μL, 2×10^6) to develop the subcutaneous tumour model. Before implantation of tumour, the feather of implantation area was shaved by shaver and depilatory cream. The orthotopic brain tumour model was prepared by implantation of luciferase-transfected human gliomas cells (U87-Luc) (5 μL, 5×10^5) into the brain of the female Balb/c nude mice using stereotaxic apparatus with a mouse adaptor (RWD, Life Science Co., Ltd), 1 μL/min a time.

In vivo imaging:

CT imaging was carried out on a Micro CT (TriFoil Imaging CT120) with fast scan mode. MR imaging was performed on a MRI scanner (MR solution, 3T) using T_2 sequence. Bioluminescence imaging was performed on an IVIS Spectrum optical imaging system (PerkinElmer, USA). MPI was imaged using a MPI scanner (Magnetic Insight Inc, MOMENTUM™ Imager). Photoacoustic imaging was conducted on a photoacoustic imaging system (Vevo LAZR, Visual Sonics Company, Canada). The detailed parameters for imaging are described in supporting information.

In vivo hyperthermia therapy:

Photothermal therapy *in vivo.* Mice bearing 4T1 tumours were divided into four groups (five mice in each group.): 1 x PBS, NIR (1064 nm laser only), FeCo@C-PEG only (i. t. injection, 50 μL, 2 mg/mL), and FeCo@C-PEG (i. t. injection, 50 μL, 2 mg/mL) + 1064 nm laser. Two hours later, a 1640 nm continuous laser (Hi-Tech Optoelectronics Co., Ltd. Beijing) was employed to irradiate tumours for 10 min (1.0 W/cm^2), post injection of FeCo@C-PEG. Meanwhile, the tumour temperatures were recorded by an infrared thermal camera (IRS E50 Pro Thermal Imaging Camera). The tumour sizes were recorded every 2 days after treatment, the volume = (tumour length) × (tumour width)^2/2. The relative volumes were expressed as V/V_0 (V_0 was the initial tumour volume).

Magnetic hyperthermia therapy *in vivo:*

Mice bearing 4T1 tumours were divided into four groups (n = 5) and treated with (1) 1 x PBS, (2) only magnetic field, (3) only FeCo@C-PEG only (i. t. injection, 50 μL, 5 mg/mL), and (4) FeCo@C-PEG (i. t. injection, 50 μL, 5 mg/mL) and magnetic field. Two hours later, a magnetic hyperthermia coil setup (Shenzhen Shuanping Power Supply Technology Co., Ltd., SP-15A, 100 kHz, 30 kA/m, 15 KVA) was placed over the tumours and applied an

alternating current magnetic field to heat the tumours for 10 min. 24 h after treatment, the tumour tissues in each group were collected for Hematoxylin and Eosin (H&E) staining, and then examined by a Leica DM4 B microscope (Leica Microsystems GmbH, Wetzlar, Germany).

Reporting summary.

Further information on research design is available in the Nature Research Reporting Summary linked to this article.

Supplementary Material

Refer to Web version on PubMed Central for supplementary material.

Acknowledgements

The authors acknowledge the use of Stanford Centre for Innovation in In-Vivo Imaging (SCI3) Core Facility. This work was supported by the Stanford University National Cancer Institute (NCI) CCNE-T grant (U54CA199075).

References

1. Smith BR & Gambhir SS Nanomaterials for in vivo imaging. Chem. Rev 117, 901–986 (2017). [PubMed: 28045253]
2. Kunjachan S, Ehling J, Storm G, Kiessling F. & Lammers T. Noninvasive imaging of nanomedicines and nanotheranostics: principles, progress, and prospects. Chem. Rev 115, 10907–10937 (2015). [PubMed: 26166537]
3. Signore A, Mather SJ, Piaggio G, Malviya G. & Dierckx RA Molecular imaging of inflammation/infection: nuclear medicine and optical imaging agents and methods. Chem. Rev 110, 3112–3145 (2010). [PubMed: 20415479]
4. Louie A. Multimodality imaging probes: design and challenges. Chem. Rev 110, 3146–3195 (2010). [PubMed: 20225900]
5. Wu L, Mendoza-Garcia A, Li Q. & Sun S. Organic phase syntheses of magnetic nanoparticles and their applications. Chem. Rev 116, 10473–10512 (2016).
6. Gleich B. & Weizenecker J. Tomographic imaging using the nonlinear response of magnetic particles. Nature 435, 1214–1217 (2005). [PubMed: 15988521]
7. Goodwill PW, et al. X-space MPI: magnetic nanoparticles for safe medical imaging. Adv. Mater 24, 3870–3877 (2012). [PubMed: 22988557]
8. Lemaster JE, Chen F, Kim T, Hariri A. & Jokerst JV Development of a trimodal contrast agent for acoustic and magnetic particle imaging of stem cells. ACS Appl. Nano Mater 1, 1321–1331 (2018).
9. Ludewig P, et al. Magnetic particle imaging for real-time perfusion imaging in acute stroke. ACS Nano 11, 10480–10488 (2017).
10. Tay ZW, et al. Magnetic particle imaging-guided heating in vivo using gradient fields for arbitrary localization of magnetic hyperthermia therapy. ACS Nano 12, 3699–3713 (2018). [PubMed: 29570277]
11. Yu EY, et al. Magnetic particle imaging for highly sensitive, quantitative, and safe in vivo gut bleed detection in a murine model. ACS Nano 11, 12067–12076 (2017).
12. Arami H, et al. In vivo multimodal magnetic particle imaging (MPI) with tailored magneto/optical contrast agents. Biomaterials 52, 251–261 (2015). [PubMed: 25818431]
13. Ferguson RM, et al. Magnetic particle imaging with tailored iron oxide nanoparticle tracers. IEEE T. Med. Imaging 34, 1077–1084 (2015).
14. Yu EY, et al. Magnetic particle imaging: a novel in vivo imaging platform for cancer detection. Nano Lett. 17, 1648–1654 (2017). [PubMed: 28206771]

15. Song G, et al. Janus iron oxides@semiconducting polymer nanoparticle tracer for cell tracking by magnetic particle imaging. Nano Lett. 18, 182–189 (2018). [PubMed: 29232142]
16. Pablico-Lansigan MH, Situ SF & Samia AC Magnetic particle imaging: advancements and perspectives for real-time in vivo monitoring and image-guided therapy. Nanoscale 5, 4040–4055 (2013). [PubMed: 23538400]
17. Tomitaka A, Arami H, Gandhi S. & Krishnan KM Lactoferrin conjugated iron oxide nanoparticles for targeting brain glioma cells in magnetic particle imaging. Nanoscale 7, 16890–16898 (2015).
18. Zheng B, et al. Magnetic particle imaging tracks the long-term fate of in vivo neural cell implants with high image contrast. Sci. Rep 5, 14055 (2015).
19. Zheng B, et al. Quantitative magnetic particle imaging monitors the transplantation, biodistribution, and clearance of stem cells in vivo. Theranostics 6, 291–301 (2016). [PubMed: 26909106]
20. Du Y, Liu X, Liang Q, Liang XJ & Tian J. Optimization and design of magnetic ferrite nanoparticles with uniform tumour distribution for highly sensitive MRI/MPI performance and improved magnetic hyperthermia therapy. Nano Lett, 19, 3618–3626 (2019). [PubMed: 31074627]
21. Arami H. & Krishnan KM Intracellular performance of tailored nanoparticle tracers in magnetic particle imaging. J. Appl. Phys 115, 17B306 (2014).
22. Khandhar AP, et al. Evaluation of PEG-coated iron oxide nanoparticles as blood pool tracers for preclinical magnetic particle imaging. Nanoscale 9, 1299–1306 (2017). [PubMed: 28059427]
23. Arami H, Ferguson RM, Khandhar AP & Krishnan KM Size-dependent ferrohydrodynamic relaxometry of magnetic particle imaging tracers in different environments. Med. Phys 40, 071904 (2013).
24. Bauer LM, Situ SF, Griswold MA & Samia AC Magnetic particle imaging tracers: State-of-the-art and future directions. J. Phys. Chem. Lett 6, 2509–2517 (2015). [PubMed: 26266727]
25. Ferguson MR, Minard KR & Krishnan KM Optimization of nanoparticle core size for magnetic particle imaging. J. Magn. Magn. Mater 321, 1548–1551 (2009). [PubMed: 19606261]
26. Zheng B, et al. Seeing SPIOs directly in vivo with magnetic particle imaging. Mol. Imaging Biol 19, 385–390 (2017). [PubMed: 28396973]
27. Gu E, Chen W-Y, Gu J, Burridge P. & Wu JC Molecular imaging of stem cells: tracking survival, biodistribution, tumorigenicity, and immunogenicity. Theranostics 2, 335–345 (2012). [PubMed: 22509197]
28. Seo WS, et al. FeCo/graphitic-shell nanocrystals as advanced magnetic-resonance-imaging and near-infrared agents. Nat. Mater 5, 971–976 (2006). [PubMed: 17115025]
29. Yu J, et al. Multifunctional Fe_5C_2 nanoparticles: a targeted theranostic platform for magnetic resonance imaging and photoacoustic tomography-guided photothermal therapy. Adv. Mater 26, 4114–4120 (2014). [PubMed: 24677251]
30. Gao J, et al. Multifunctional yolk-shell nanoparticles: a potential MRI contrast and anticancer agent. J. Am. Chem. Soc 130, 11828–11833 (2008).
31. Zeng J, et al. Anchoring group effects of surface ligands on magnetic properties of Fe_3O_4 nanoparticles: towards high performance MRI contrast agents. Adv. Mater 26, 2694–2698 (2014). [PubMed: 24615901]
32. Song G, et al. Core-shell MnSe@Bi_2Se_3 fabricated via a cation exchange method as novel nanotheranostics for multimodal imaging and synergistic thermoradiotherapy. Adv. Mater 27, 6110–6117 (2015). [PubMed: 26331476]
33. Sun X, et al. Separation of nanoparticles in a density gradient: FeCo@C and gold nanocrystals. Angew. Chem. Int. Ed 48, 939–942 (2009).
34. Chen Z, et al. Graphite-coated magnetic nanoparticle microarray for few-cells enrichment and detection. ACS Nano 6, 1094–1101 (2012). [PubMed: 22229344]
35. Li Y, et al. In situ targeted MRI detection of Helicobacter Pylori with stable magnetic graphitic nanocapsules. Nat. Commun 8, 15653 (2017).
36. Roper DK, Ahn W. & Hoepfner M. Microscale heat transfer transduced by surface plasmon resonant gold nanoparticles. J. Phys. Chem. C 111, 3636–3641 (2007).

37. Qiwei T, et al. Hydrophilic Cu_9S_5 nanocrystals: a photothermal agent with a 25.7% heat conversion efficiency for photothermal ablation of cancer cells in vivo. ACS Nano 5, 9761–9771 (2011). [PubMed: 22059851]
38. Kaul MG, et al. In vitro and in vivo comparison of a tailored magnetic particle imaging blood pool tracer with Resovist. Phys. Med. Biol 62, 3454–3469 (2017). [PubMed: 28060771]
39. Espinosa A, et al. Magnetic (hyper)thermia or photothermia? Progressive comparison of iron oxide and gold nanoparticles heating in water, in cells, and in vivo. Adv. Funct. Mater 28, 1803660 (2018).
40. Reimer P. & Balzer T. Ferucarbotran (Resovist): a new clinically approved RES-specific contrast agent for contrast-enhanced MRI of the liver: properties, clinical development, and applications. Eur. Radiol 13, 1266–1276 (2003). [PubMed: 12764641]
41. Kircher MF, et al. A brain tumour molecular imaging strategy using a new triple-modality MRI-pphotoacoustic-Raman nanoparticle. Nat. Med 18, 829–834 (2012). [PubMed: 22504484]
42. Wu J, et al. Semiconducting polymer nanoparticles for centimeters-deep photoacoustic imaging in the second near-infrared window. Adv. Mater 29, 1703403 (2017).
43. Kim T, Lemaster JE, Chen F, Li J. & Jokerst JV Photoacoustic imaging of human mesenchymal stem cells labeled with Prussian Blue-poly(l-lysine) nanocomplexes. ACS Nano 11, 9022–9032 (2017). [PubMed: 28759195]
44. Kang J, et al. Enhanced performance of a molecular photoacoustic imaging agent by encapsulation in mesoporous silicon nanoparticles. Adv. Mater 30, 1800512 (2018).
45. Hong G, Antaris AL & Dai H. Near-infrared fluorophores for biomedical imaging. Nat. Biomed. Eng 1, 0010 (2017).
46. Espinosa A, et al. Duality of iron oxide nanoparticles in cancer therapy: amplification of heating efficiency by magnetic hyperthermia and photothermal bimodal treatment. ACS Nano 10, 2436–2446 (2016). [PubMed: 26766814]
47. Zhou J, et al. Compact plasmonic blackbody for cancer theranosis in the near-infrared II window. ACS Nano 12, 2643–2651 (2018). [PubMed: 29438610]
48. Zhang J, et al. Activatable photoacoustic nanoprobes for in vivo ratiometric imaging of peroxynitrite. Adv. Mater 29, 1604764 (2017).
49. Shang W, et al. Core-shell gold nanorod@metal-organic framework nanoprobes for multimodality diagnosis of glioma. Adv. Mater 29, 1604381 (2017).
50. Kim DJ, Pal M. & Seo WS Confined growth of highly uniform and single bcc-phased FeCo/graphitic-shell nanocrystals in SBA-15. Micropor. Mesopor. Mat 180, 32–39 (2013).
51. Hao J, et al. In vivo long-term biodistribution, excretion, and toxicology of PEGylated transition - metal dichalcogenides MS2 (M = Mo, W, Ti) nanosheets. Adv. Sci 4, 1600160 (2017).
52. Yu M. & Zheng J. Clearance pathways and tumour targeting of imaging nanoparticles. ACS Nano 9, 6655–6674 (2015). [PubMed: 26149184]

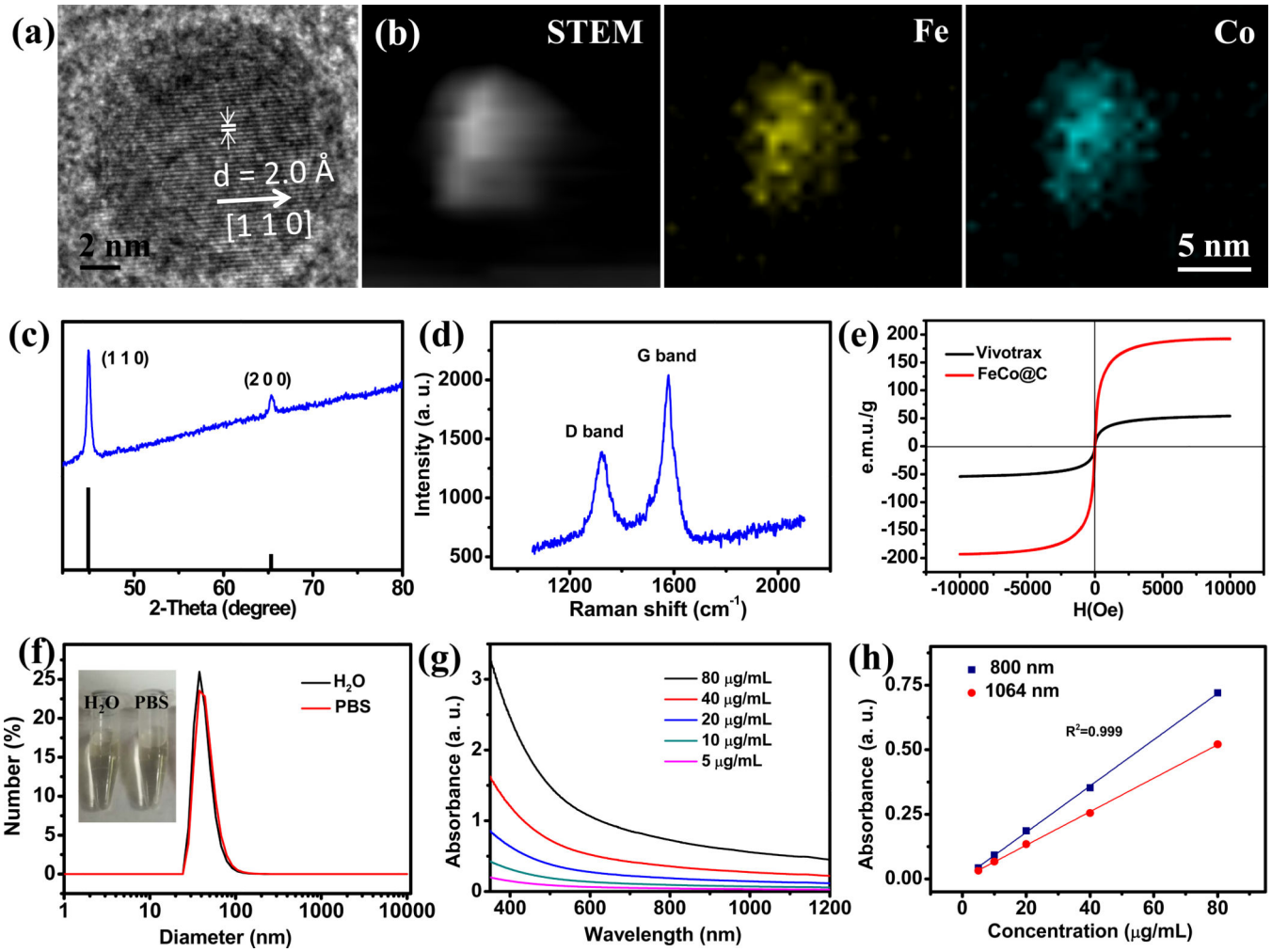

Fig. 1 |. Characterization of 10 nm FeCo@C-PEG purified by density gradient separation (Fraction #3).

a, High resolution TEM image. **b**, STEM image and element mapping. **c**, XRD patterns of FeCo@C-PEG (blue curve) and standard peaks (black) of cubic FeCo (PDF#49–1567). **d**, Raman spectrum shows G peak (~1,578 cm^{-1}) and D peak (~1,328 cm^{-1}), confirming the presence of a graphitic carbon shell. **e**, Magnetic hysteresis curve of FeCo@C-PEG (red curve) and Vivotrax (black curve). **f**, DLS size of FeCo@C-PEG in 1 x PBS and water (inset: photograph of tubes containing FeCo@C-PEG in 1 x PBS and water). **g**, UV-Vis-NIR absorbance spectra of FeCo@C-PEG at indicated concentrations in water. **h**, Plots of linear fitting absorbance at 800 nm and 1064 nm for FeCo@C-PEG over concentrations in water.

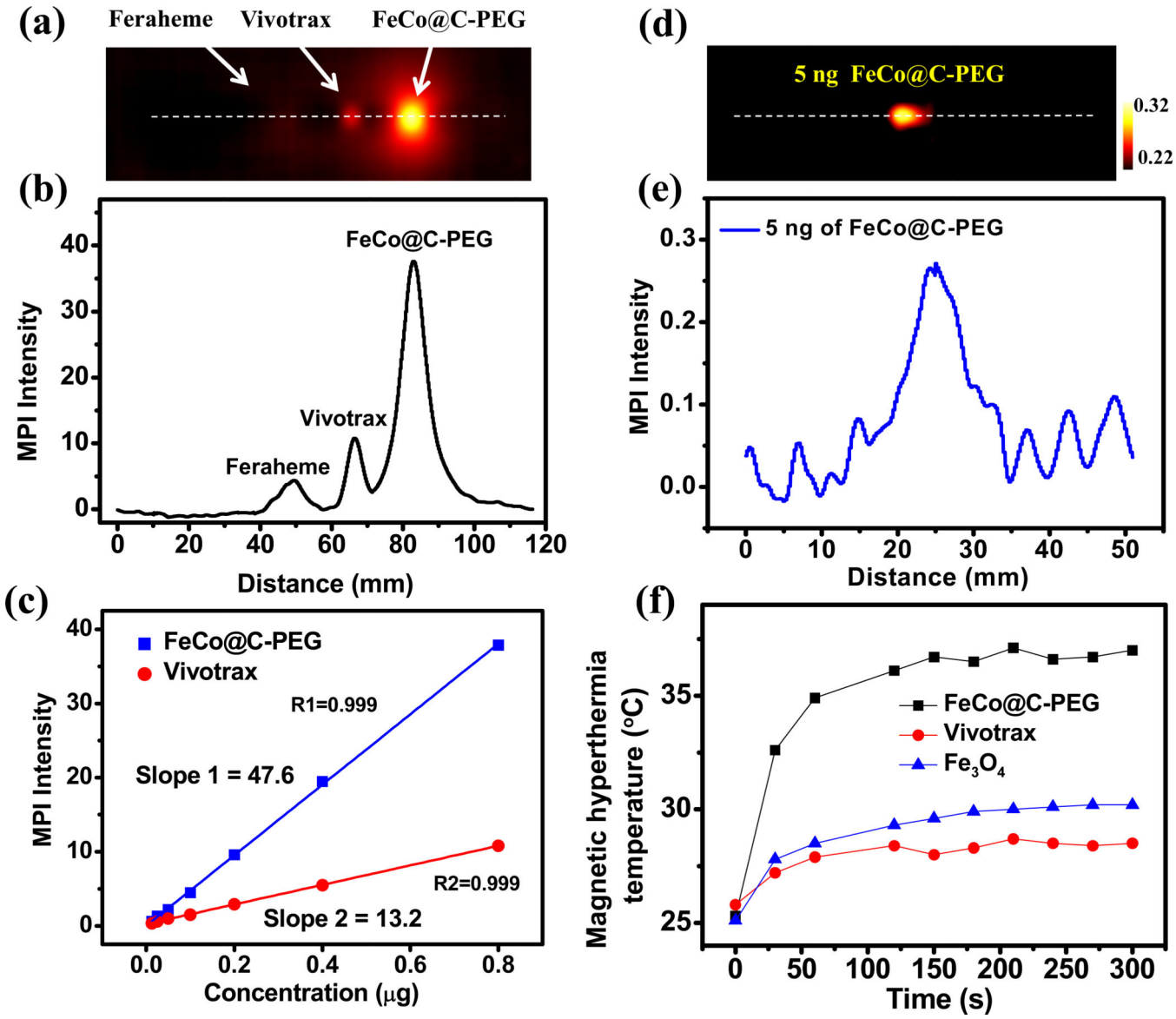

Fig. 2 |. *In vitro* magnetic particle imaging and magnetic hyperthermia by FeCo@C-PEG (Fraction #3).

a, 2-D projection MPI image of FeCo@C-PEG (Fraction #3), Vivotrax and Feraheme (800 ng of core) in PCR tubes. **b**, MPI point-of-spread function (PSF) of image in **a**. **c**, Plot of the MPI signals of FeCo@C-PEG (Fraction #3) and Vivotrax versus the mass of nanoparticles' core. **d**, 2D Average MPI images (25 times scanning) of PCR tube containing FeCo@C-PEG (5 ng of core) after background subtraction. **e**, PSF of MPI image in **d**. **f**, Magnetic hyperthermia heating curves of FeCo@C-PEG (Fraction #3), Vivotrax and Fe_3O_4 nanoparticles (4 mg/mL, nanoparticles' core), measured inside the magnetic hyperthermia coil setup (100 kHz, 15 KVA).

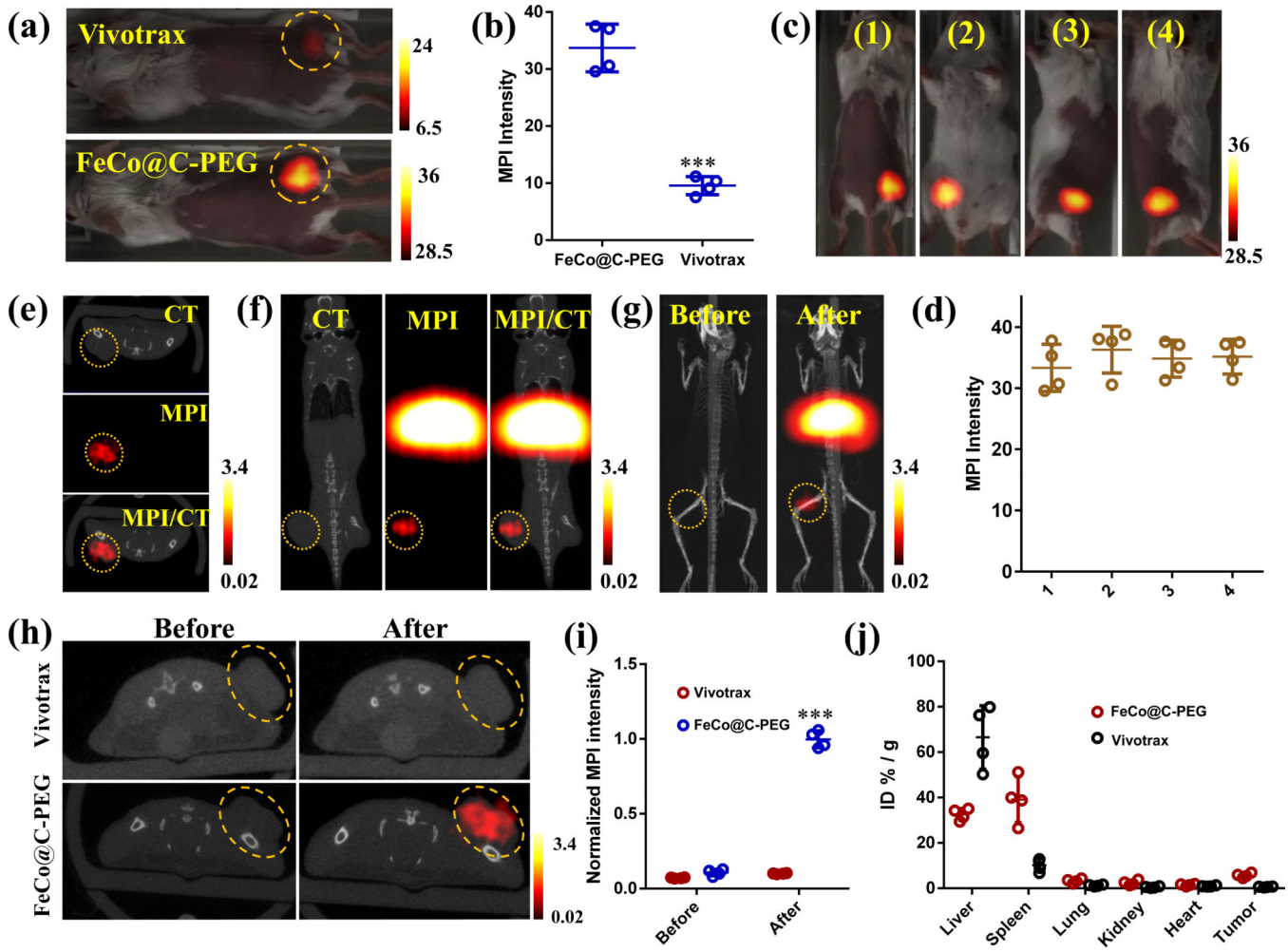

Fig. 3 |. *In vitro* magnetic particle imaging of FeCo@C-PEG (Fraction #3) in mice.

a, 2-D projection MPI images of mice bearing 4T1 xenograft breast tumours intratumourally injected with 20 μL of FeCo@C-PEG (35 μg/mL) or Vivotrax (35 μg/mL). **b**, Quantification of total MPI signals of tumour areas in a (Two-tailed Student's t-test, ***P = 0.00041, error bars represent mean ± s. d., n = 4). **c**, 2-D projection MPI images of mice from different views, after intratumoural injection of FeCo@C-PEG (20 μL, 35 μg/mL). **d**, Quantification of total MPI signals of tumour areas in **c**. **e-i**, MPI and CT imaging of mice bearing 4T1 xenograft breast tumours received i. v. injection of FeCo@C-PEG or Vivotrax (3 mg/kg). **e, f**, CT, MPI, and CT/MPI images of mice 24 hours after injection of FeCo@C-PEG: **e**, axial direction; **f**, coronal direction. **g**, 3-D CT/MPI images of mice before and after injection of FeCo@C-PEG nanoparticles. **h**, Axial CT/MPI images of mice before and after injection of Vivotrax or FeCo@C-PEG. **i**, Quantification of total MPI signals of tumour areas before and after injection of Vivotrax and FeCo@C-PEG (Two-tailed Student's t-test, ***P = 0.00012, error bars represent mean ± s. d., n = 4). **j**, *Ex vivo* biodistribution of FeCo@C-PEG in main organs after injection of indicated MPI tracer.

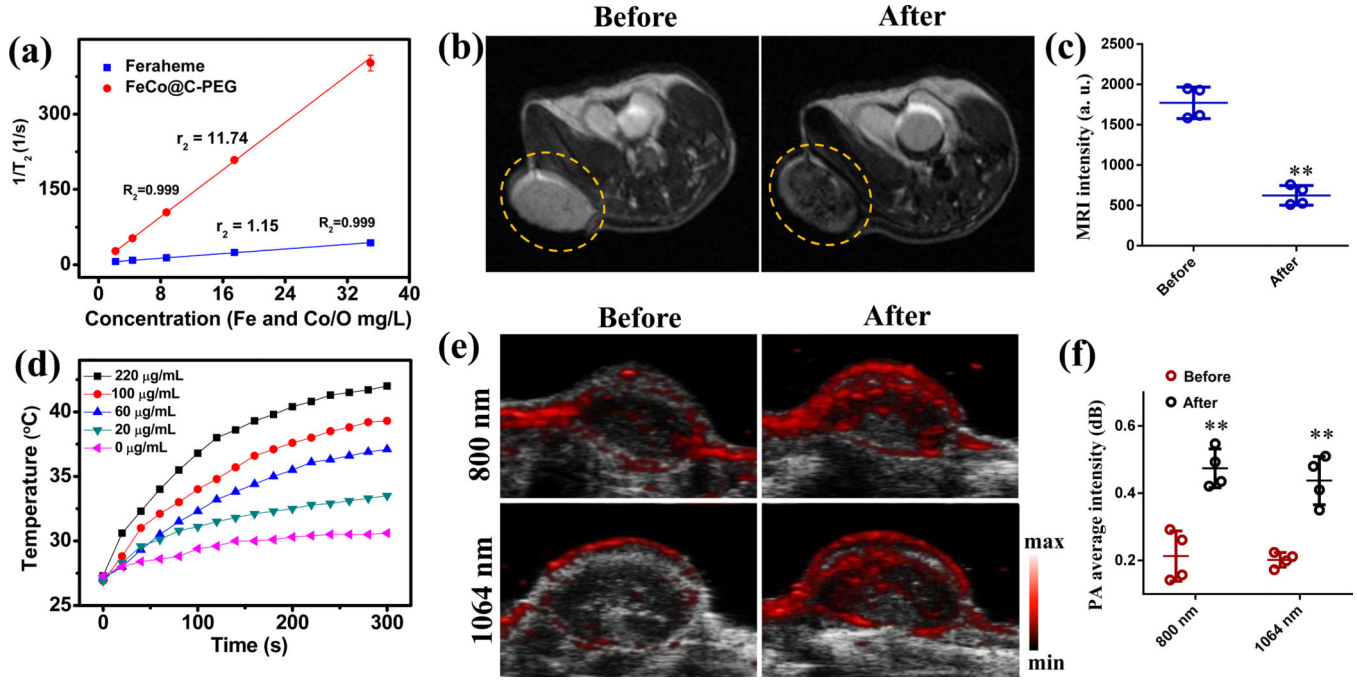

Fig. 4 |. Magnetic resonance imaging and photoacoustic imaging with FeCo@C-PEG.

a, T_2 relaxation rate ($1/T_2$) of Feraheme and FeCo@C-PEG solutions as the function of core concentrations. **b**, MRI images of mice bearing 4T1 xenograft breast tumours before and 24 hours after i.v. injection of FeCo@C-PEG (3 mg/kg). **c**, Quantification of MRI signals of tumour areas before and after injection of FeCo@C-PEG (Two-tailed Student's t-test, **P = 0.0054, error bars represent mean ± s. d., n = 4). **d**, Photothermal heating curves of FeCo@C-PEG with different concentrations under a 1064 nm laser irradiation (1.0 W^2/cm). **e, f**, The mice bearing 4T1 tumours were scanned by PA scanner at 800 and 1064 nm laser excitation before and 24 hours after i.v. injection of FeCo@C-PEG (3 mg/kg): **e**, US/PA images scanned; **f**, corresponding quantification of average PA signals of tumour areas before and after injection of FeCo@C-PEG at 800 nm and 1064 nm of laser excitation (Two-tailed Student's t-test, ** P = 0.0092 for 800 nm, ** P = 0.0030 for 1064 nm, error bars represent mean ± s. d., n = 4).

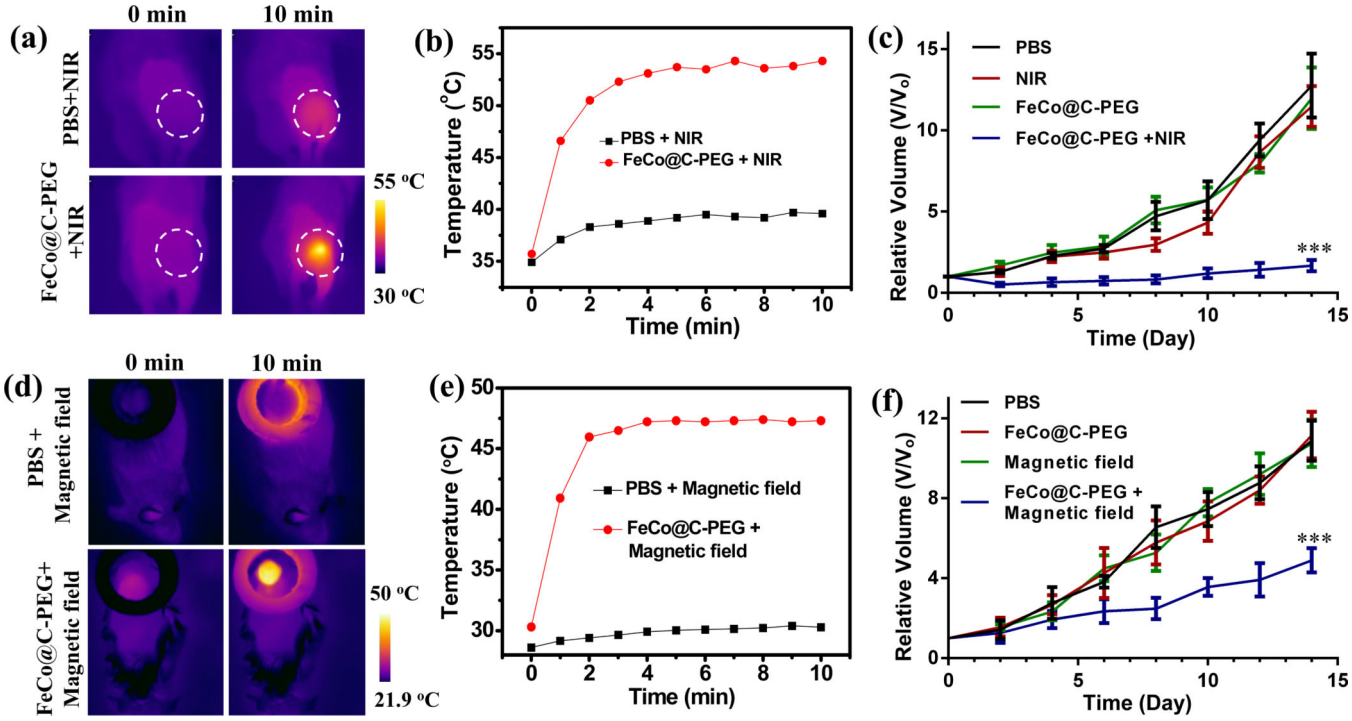

Fig. 5 |. *In vivo* magneto/photo thermal therapy with FeCo@C-PEG.

a, IR thermal images of 4T1 tumour-bearing mice intratumourally injected with FeCo@C-PEG (100 μg) or 1 x PBS, and then exposed to the 1064 nm laser (1.0 W/cm^2) for 10 min. **b**, Photothermal heating curves of tumours monitored by the IR thermal camera, during laser irradiation. **c**, The growth curves of 4T1 tumours in mice treated with 1 x PBS injection, NIR II laser (1064 nm) only, FeCo@C-PEG only (i.t. injection, 50 μl, 2 mg/mL), or FeCo@C-PEG (i.t. injection, 50 μL, 2 mg/mL) + NIR II laser (1064 nm) (Two-tailed Student's t-test, ***P = 0.00027, error bars represent mean ± s. d., n = 5). **d-f**, *In vivo* magnetic hyperthermia therapy: **d**, infrared thermal images of tumour-bearing mice i. t. injected with FeCo@C-PEG (50 μL, 5 mg/mL) or 1 x PBS, and then heated in a magnetic coil setup (100 kHz, 15 KVA); **e**, corresponding magnetic hyperthermia heating curves of tumours monitored by the infrared thermal camera; **f**, the growth curves of 4T1 tumours in mice treated with 1 x PBS, Magnetic field (100 kHz, 15 KVA) only, FeCo@C-PEG only (i.t. injection, 50 μL, 5 mg/mL), and FeCo@C-PEG (i.t. injection, 50 μL, 5 mg/mL) + Magnetic field (100 kHz, 15 KVA) (Two-tailed Student's t-test, ***P = 0.00049, error bars represent mean ± s. d., n = 5).

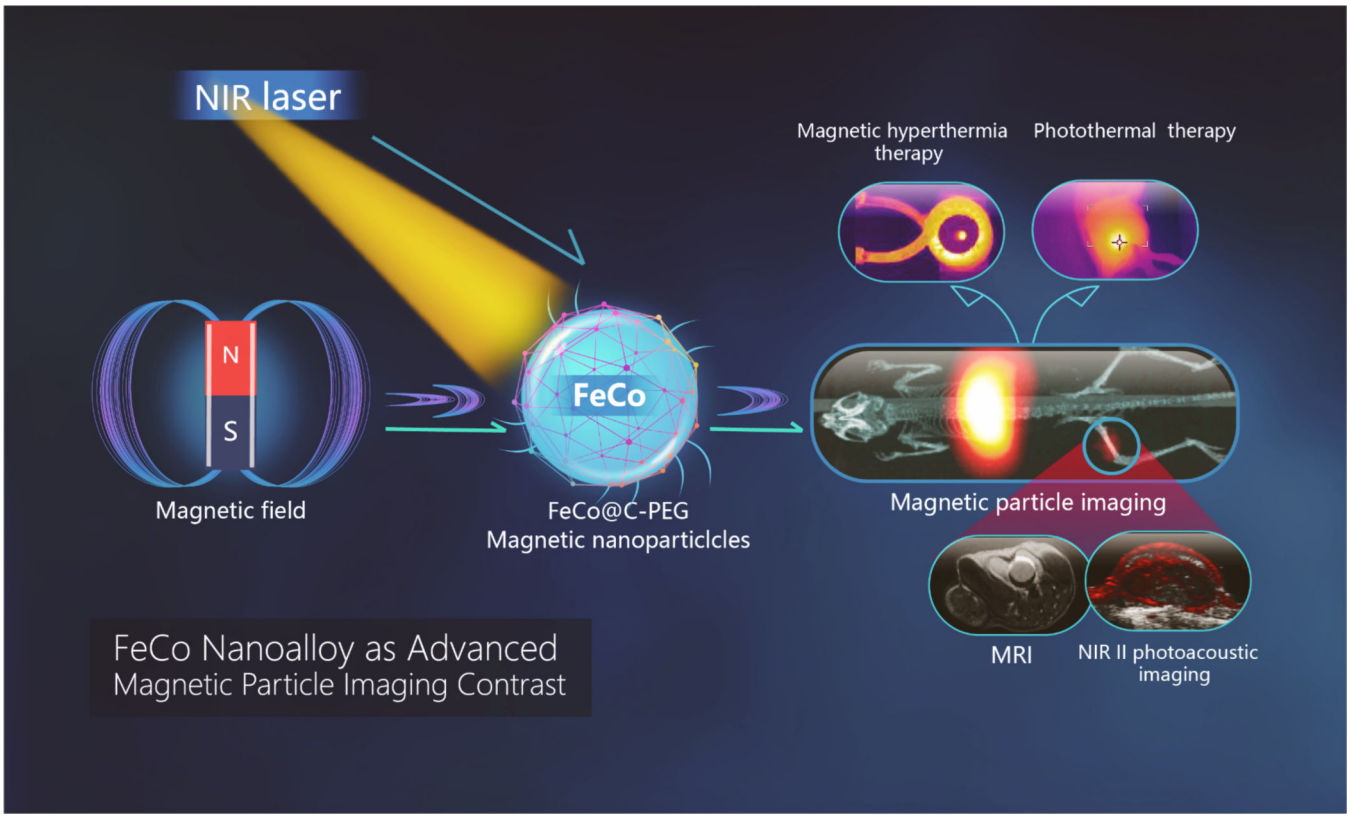

Scheme 1.

FeCo@C-PEG nanoparticles enable multiple modality imaging-MPI, MRI, near infrared II-photoacoustic imaging, and effective NIR-II photothermal and magnetic hyperthermia ablation of solid tumor.

Table 1 |

Composition of nanoparticles FeCo@C-PEG and their MPI signals.

	#1	#2	#3	#4	#5	Vivotrax
Silica : Metal (g : g)	4:1	2:1	1:1	1:1	1:1	
Fe : Co (moL : moL)	1:1	1:1	1:1	1:2	2:1	
MPI signal (1 μg of core)	12.9	14.3	32.4	25.7	18.3	13.5
MPI FeCo/ Vivotrax	0.95	1.05	2.4	1.9	1.35	1

Table 2 |

Sizes and metal ratios of nanoparticles FeCo@C-PEG purified by density gradient separation and comparison of their MPI intensities.

	#1	#2	#3	#4	#5	Vivotrax	Feraheme
Size (nm)	5.3 ± 1.5	7.1 ± 2.0	10.2 ±2.8	12.1 ±2.3	15.9 ± 5.6		
Fe : Co (moL : moL)	1: 0.46	1: 0.69	1: 0.87	1: 0.70	1: 0.73		
MPI signal (1 μg of core)	25.6	41.8	47.4	26.6	6.2	13.5	5.5
MPI FeCo / Vivotrax (same core mass)	1.89	3.09	3.51	1.97	0.46	1	
MPI FeCo/ Vivotrax (same mole of core)	2.54	4.83	6.08	3.09	0.73	1	
MPI FeCo/ Feraheme (same mass of core)	4.65	7.60	8.62	4.84	1.13		1
MPI FeCo/ Feraheme (same mole of core)	6.24	11.85	14.91	7.59	1.80		1